Supplementary information

Two-stage oxidation of petrogenic organic carbon in a rapidly exhuming small mountainous catchment

Wan-Yin Lien[1], Chih-Tung Chen[2], Yun-Hsuan Lee[1,3], Chih-Chieh Su[3,4], Pei-Ling Wang[3,4,5*], and Li-Hung Lin[1,4,5*]

[1]Department of Geosciences, National Taiwan University, Taipei 106, Taiwan
[2]Department of Earth Sciences, National Central University, Taoyuan 231, Taiwan
[3]Institute of Oceanography, National Taiwan University, Taipei 106, Taiwan
[4]Science and Technology Research Institute for Decarbonization, National Taiwan University, Taipei 106, Taiwan
[5]Research Center for Future Earth, National Taiwan University, Taipei 106, Taiwan

Corresponding author and contact info
Pei-Ling Wang, plwang@ntu.edu.tw
Institute of Oceanography
National Taiwan University
No. 1, Sec. 4, Roosevelt Rd., Taipei 106, Taiwan

Li-Hung Lin, lhlin@ntu.edu.tw
Department of Geosciences
National Taiwan University
No. 1, Sec. 4, Roosevelt Rd., Taipei 106, Taiwan

Supplementary Note 1

The residence time of river sediments

The retention time of river sediments ahead of burial is a crucial factor for OC_{petro} oxidation[1]. Suspended load travels roughly at or slightly lags behind the velocity of stream while most bedload experiences protracted transports perturbed by intermittent discharge pulse (i.e., floods in typhoon season). Although no estimation about the residence times of these two sediment categories in the Beinan catchment has been reported to our knowledge, previous studies provide some constraints. Based on the variation in water discharge and suspended load, the removal of suspended load from mass wasting in the drainage basin has been estimated to be complete from within days to a month in rivers originating from the eastern Backbone Range[2]. Furthermore, the evacuation time for bedload in Peikang River derived from the landslide induced by M_w = 7.6 Chi-Chi earthquake in western Taiwan has been estimated to take 10 to 600 yr[3]. As the bedload transport rate q_s is positively correlated to the stream power ω ($q_s \propto \omega$), the rate ratio for the Beinan to Peikang River was estimated using the following relationship[4]:

$$\omega = \rho_w \, g \, (\frac{Q}{W}) \, S \qquad \text{eq. S1}$$

where ρ_w is the water density, g is the gravitational acceleration, Q is the average annual discharge, W is the channel width, and S is the slope. The transport rate ratio for bedload was, therefore, estimated based on the W of 60 m for Peikang vs. 30 m for Beinan, Q of 26.9 cms for Peikang (statistics for 1976–2022) vs. 92.6 cms for Beinan (statistics for 1941–2022), and S of 0.015 for Peikang vs. 0.028 for Beinan[5] (open data from Water Resources Agency). The computation yields that the bedload transport rate for Beinan River is 12 times greater than Peikang River. In this regard, the residence time for bedload in the Beinan catchment may last for from within one year (10/12 = 0.8) to decades. Taken together, the short time scales and similar maturities of OC_{petro} between bedload and suspended load (Figs. 3d and 3e) suggest that OC_{petro} remains unaltered from physical erosion and biogeochemical processes in fluvial systems.

Supplementary Note 2

The provenance of OC_{petro} in river sediments

Considering that the degradation during river transit and contribution of weathered materials to river sediments were negligible (Fig. 3), the Raman parameters for river sediments would represent the collective signatures indicative of upstream source rocks. The 1-D histogram of temperature distribution derived from Raman parameters has

been utilized to trace the provenance of river sediments and to explore the exhumation history of orogens[6,7]. To better test and visualize the variation in the source of river sediments, a new parameter, Raman distance, defined as the normalized distance between the maturities for weathered products/river sediments and the average for all rocks in the plot of total width versus calculated temperature (Fig. 3), was introduced to provide a measure that quantifies the integrated characteristics of Raman spectra. The utility of the Raman distance was verified by comparing the values of rock and bedload samples with the lithological distribution (Fig. 1a). Using this approach, the negative Raman distance represents more disordered OC_{petro} than the average maturities of rocks, and vice versa.

Our calculations yields that most Raman distances for river sediments are between the range of bedrocks (0.08±0.09 for schist and -0.08±0.09 for slate; Fig. S4). However, Raman distances for OC_{petro} from rocks and river sediments at the same sites diverge. For one category, the Raman distances for river sediments at LD, MLL and DLKW are less than local rocks. At these sites, the lithologies are mainly composed of rocks with relatively high metamorphic grade (meta-sandstone for LD, the boundary between the schist and slate formations for MLL, and the boundary between the schist and metagranite for DLKW). However, the individual drainage basins beyond the sampling site are extended to the region of the slate formation or less mature schist zone (for DLKW) (Fig. 1). Therefore, the low Raman distances are consistent with the limited supply of sediments eroded from local lithologies and the high contribution from the upstream slate belt. For the other category, the Raman distances for river sediments are larger than those for rocks at LUL and LY. The sampling sites of LUL and LY are both located in the slate belt and away from the upstream schist belt with varying distances. As the upstream of the LUL drainage basin is confined within the schist belt, the Raman distances of LUL sediments dominated by schist characteristics clearly indicate the predominance of contributions from schist over slate (Fig. 1a). In contrast, 60% of the LY catchment drains through the slate belt, and the remaining 40% extends to the schist belt. Therefore, the dispersive Raman distances of LY sediments between typical slate and schist values correspond to comparable contributions from both upstream schist and slate formations.

In summary, the consistency between the Raman distance pattern and lithological distribution confirms the utility of Raman distance as an effective provenance index to infer the lithologic erodibility and coverage in different compartments of a small drainage basin hosted by various grades of metamorphic pelitic rocks. Conventional approaches toward provenance inference often rely on the identification of sediment lithologies or index minerals, or the distribution of detrital zircon U-Pb ages[8]. These approaches could have either been biased by selective preservation against fine-grained

particulates during river transit or suffered from incomplete resetting of inherited signals by the target metamorphism. The Raman distance described in this study offers a rapid and semi-quantifiable provenance index particularly useful for fine grained particulates that originated from metamorphic pelitic rocks and experienced short-lived metamorphism. It also bears great potential to be extrapolated to a larger drainage basin with more complex geological compositions or records that preserve the dynamic exhumation history of a metamorphic terrane.

Supplementary Note 3

Comparison between f_{ox} and Raman parameters

To assess whether Raman parameters can be quantitatively correlated to compositional data, the correlation between f_{ox} and Raman data was examined (Fig. S5). These parameters include the derived temperature based on the relative area of D and G bands, the total width of D and G bands, and the Raman distance based on the maturity difference assessed by the total width and derived temperature between individual analyzed particle versus the averaged rock characteristics. No correlation was found between these two datasets, suggesting compositional complexity of the entire OC entity (Supplementary Discussion 1). Since Raman data provide the ordering status of individual OC_{petro} particles, both datasets may be better correlated only when graphitic carbon dominates the OC pool. In summary, the current model for OC_{petro} oxidation is limited by the lack of detailed characterization of the target organic entities using various spectroscopic and compositional analyses. It is also essential to experimentally resolve the reaction pathway and kinetics for the oxidation of graphitic carbon under ambient conditions, and to validate the collected parameters in field observations.

Supplementary Note 4

CO_2 flux from OC_{petro} oxidation during soil development

The OC_{petro} oxidation flux was estimated using the following equation:

$$\text{Oxidation flux} = TOC_{bedrock} \times f_{ox} \times \rho_r \times r \qquad \text{eq. S2}$$

where $TOC_{bedrock}$ represents the average of total organic content for slate (0.28%) and schist (0.53%), and f_{ox} is the oxidation fraction of OC_{petro} (0.65 ± 0.12 for slate and 0.49 ± 0.29 for schist), ρ_r represents rock density (assumed to be 2.8 g cm^{-3}), and r is erosion rate. The error of each variable is propagated to generate the uncertainty of the oxidation flux. The erosion/denudation rate varies substantially, depending on the time scale inherited by individual methodologies. On a decadal time scale, the erosion rate based

on riverine sediment yield has been estimated to be 20.9 mm yr^{-1} [9]. This rate could have been further refined to a range of 4–5 mm yr^{-1} using the alternative rating curve that has been considered to better cover the possible discharge range[10]. Over a millennium time scale, the denudation rate based on the exposure age derived from cosmogenic ^{10}Be has been reported to be 4.54 ± 1.86 mm yr^{-1} [11]. For comparison, the sediment accumulation rate constrained by zircon U-Pb ages has been estimated to be 5.14 mm yr^{-1} over the recent ~2 Ma[12]. The million-year scale exhumation rate based on fission-track thermochronology has been estimated to be 1.5–10 mm yr^{-1} [9]. In this regard, the erosion rate of 4.5 ± 1 mm yr^{-1} was arbitrarily chosen to accommodate a considerable range of rates derived from different methodologies across contemporary-geological time scales. Considering that OC_{petro} oxidation is also strongly tied to the landscape and climate that have been comparable with modern characteristics in the investigated catchment for thousands of years, the designated rate (4.5 ± 1 mm yr^{-1}) may be even more reliable. Using the eq. S2 and the average $TOC_{bedrock}$, the carbon fluxes were calculated to be 23 ± 7 tC km^{-2} yr^{-1} for slate and 33 ± 21 tC km^{-2} yr^{-1} for schist. If the variation in $TOC_{bedrock}$ (0.28 ± 0.23% for slate and 0.53 ± 0.39% for schist) is taken into account, the oxidation flux would exhibit a much broader range. At this stage, the computed flux is still variable primarily owing to the availability and spatial coverage of individual parameters. More data would be helpful to determine whether the consensus of computed fluxes could be reached.

Supplementary Discussion 1

The interpretation and justification of Raman and compositional data

The Raman and isotopic data are likely not referred to the same structural or chemical entities. Raman spectroscopy qualitatively characterizes the ordering status of graphitic carbon; therefore, the change in Raman maturity is primarily attributed to the residual graphitic carbon that experienced abrasion and weathering processes. In particular, broadened and stronger defect bands are generally interpreted as the formation of functional groups or alteration of graphitic structures. For example, previous experimental studies on the oxidation of highly-ordered graphite at high temperature (≥200 °C) suggest that D bands become more evident with the formation of transitional functional groups (e.g., C=O and C–O) and mass loss over a course of temperature increase[13,14]. The introduction of initial defects and functional groups further lowers the starting temperature corresponding to substantial mass loss and leads to more rapid and pronounced weight loss. In addition, soot (a highly disordered form of graphitic carbon) could be readily oxidized with concurrent CO_2 production over a heating course[15]. The soot with less ordered structure also tends to be oxidized at a faster pace than the rather ordered one, leaving the residual soot characterized by more

ordered structure. Although lab-scale experiments are conducted under dry conditions at high temperature, the experimental results provide lines of evidence that may be further extrapolated to the biologically mediated scenario under ambient conditions. First, the increasing intensity of D bands over the heating process points directly to the conversion of highly crystalline graphite into disordered form, a pattern resembling the weathering of OC_{petro} along the rock-soil transition. The experimental spectroscopic shift combined with the mass loss further suggests that the OC_{petro} could have been altered with the production of volatiles. Considering that oxygen-containing functional groups are also concomitantly produced during the experimental oxidation, CO_2 appears to be the most viable and probable candidate for volatile phase even though corresponding validation still lacks. Second, the experiments on soot lead to a higher abundance of more mature graphitic carbon and co-production of CO_2. Both preconditioned graphite and soot with less ordered structure are susceptible to faster mass losses than the ordered graphite and soot. This experimental data pattern is analogous to our observations for marine sediments where the abundance of disordered OC_{petro} decreases with the increasing transport distance from the shoreline.

The analogy drawn between our field observations and experimental constraints suggests that in addition to the feasibility of OC_{petro} oxidation, the OC_{petro} degradability and the resultant form of graphitic carbon preserved in soils or marine sediment are intimately related to the initial maturity of OC_{petro}, and that CO_2 is very likely the end product of OC_{petro} oxidation. What remains unclear is how OC_{petro} weathering prevails under conditions that are totally different from the experimental setup (e.g., biotic catalysis/high water activity versus dry O_2 at temperatures up to 800 ^{o}C). Equally important is the extent to which the degraded component is converted to CO_2 or other forms of intermediate state, and how alike and the proportion of residual total organic carbon could be attributed to graphitic carbon.

On the other hand, the isotopic compositions illustrate the ^{13}C and ^{14}C abundances of total organic matter that could be sourced from residual graphitic carbon, newly introduced labile OC, and any other uncharacterized form of organic carbon (e.g., biofilm). Similar to the results of this (Figs. 6 and S3) and previous studies[16], the isotopic results could be further fed into the quantitative assessment that constrains the loss of organic carbon during soil development.

In summary, neither of these methodologies delineates any form of transitional organic compound other than graphitic carbon, nor do they resolve whether and to what extent CO_2 is produced during the transformation of highly mature graphitic carbon in rocks to the disordered form in soils or during the elimination of the disordered form in marine sediments.

Supplementary Discussion 2

Assessment on the oxidation fraction of OC_{petro} in marine sediments

To evaluate the percentage of OC_{petro} in marine sediments that might have been oxidized during transport to the deep sea, three independent constraints using different parameters obtained in this or previous studies are assessed. The first approach is to quantify the change in the ratio of the disordered to total OC_{petro} from sediments near the estuary (NOR3-1) to the deep sea (MD18-3538). The threshold of the Raman parameter used to discriminate the ordered from disordered OC_{petro} is placed at the calculated temperature of ≥ 330 ℃ and total width of ≤ 140 cm^{-1}. The OC_{petro} with Raman parameters above this threshold (also the common range for bedrocks) is categorized as the ordered form, and vice versa as the disordered form. The ratios of the disordered to total OC_{petro} decrease from 66% (31/47) at NOR3-1 near the estuary, 36% (9/25) at OR1-960-C5, 27% (6/22) at OR1-967-S1, to 18% (5/28) at MD18-3538, the most distant site from the shoreline. This 48% decrease in the ratio is interpreted as the loss of disordered OC_{petro} during the transport. The estimate is susceptible to the uncertainty that the grain count provided above cannot be directly translated into mass difference. To provide a conservative assessment, this estimate could be considered as an upper bound for the oxidation of OC_{petro}. The second constraint presented in the main text is to configure the mass balance and mixing process based on the abundance and isotopic composition of OC and OC_{petro}. This approach yields the f_{ox} values of 0.65 ± 0.12 for slate and 0.49 ± 0.29 for schist. As stated in Discussion, soil development has been estimated to last for tens of years, which is comparable with the time scale for transport from the estuary to the distal abyssal plain. Considering a higher oxidative driver associated with atmospheric oxygen, this range of f_{ox} could also be regarded as an upper bound for the oxidation of OC_{petro} during marine transit. Finally, the previous study based on Re proxy has revealed the flux of riverine Re and derived OC_{petro} oxidation ranged from 11 to 22 tC km^{-2} yr^{-1} in two tributaries of the current investigated catchment[17]. Using the catchment area, sediment yield of 20 Mt yr^{-1} [10], TOC_{petro} content of 0.27% (average of TOC for BNE sediments in this study), the fraction of OC_{petro} oxidized during soil development and river transit is calculated to be 34–51%. Again, this estimate could have been larger than that for marine transit, serving as an upper bound for the OC_{petro} oxidation. In summary, the assessments framed by three different approaches enable the placement of the upper bound for the fraction of OC_{petro} oxidation to be less than 34%. For a conservative estimate, the oxidation flux along marine transit is constrained by using an oxidation fraction of 1% to demonstrate that the magnitude of OC_{petro} oxidation in marine environments cannot be neglected.

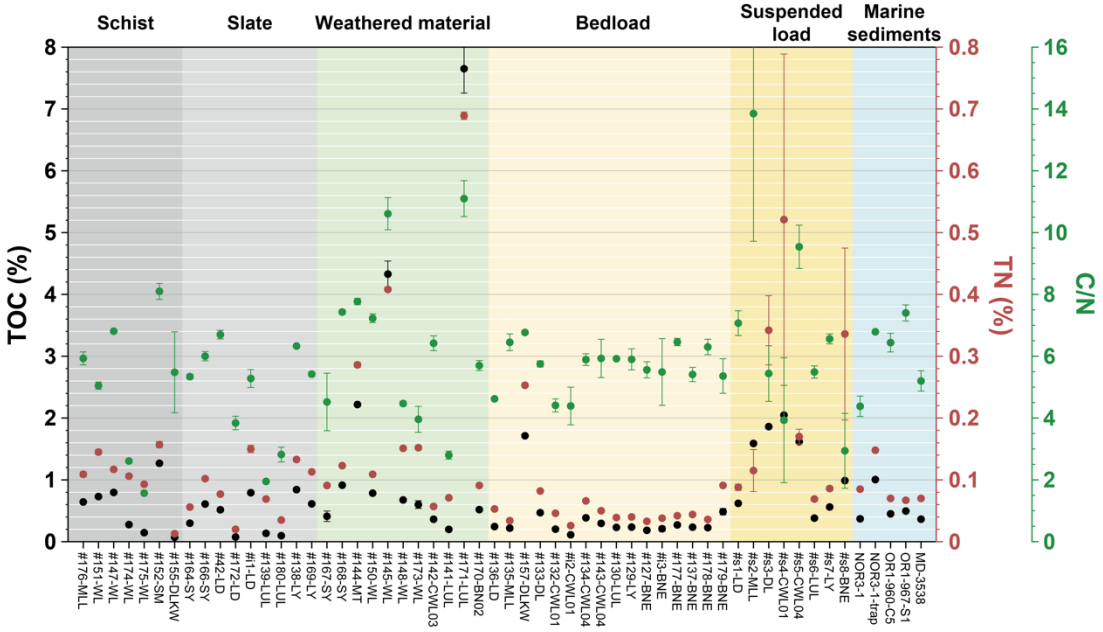

Fig. S1. TOC, TN and C/N values of all collected samples.

Black, red and green color each represents TOC and TN concentrations and C/N ratio, respectively. Shaded areas distinguish samples by type. The TOC and TN contents and standard deviations were determined by at least duplicate aliquots of each sample depending on the variation of replicates. All error bars are shown as ± 1σ (details in Table S1).

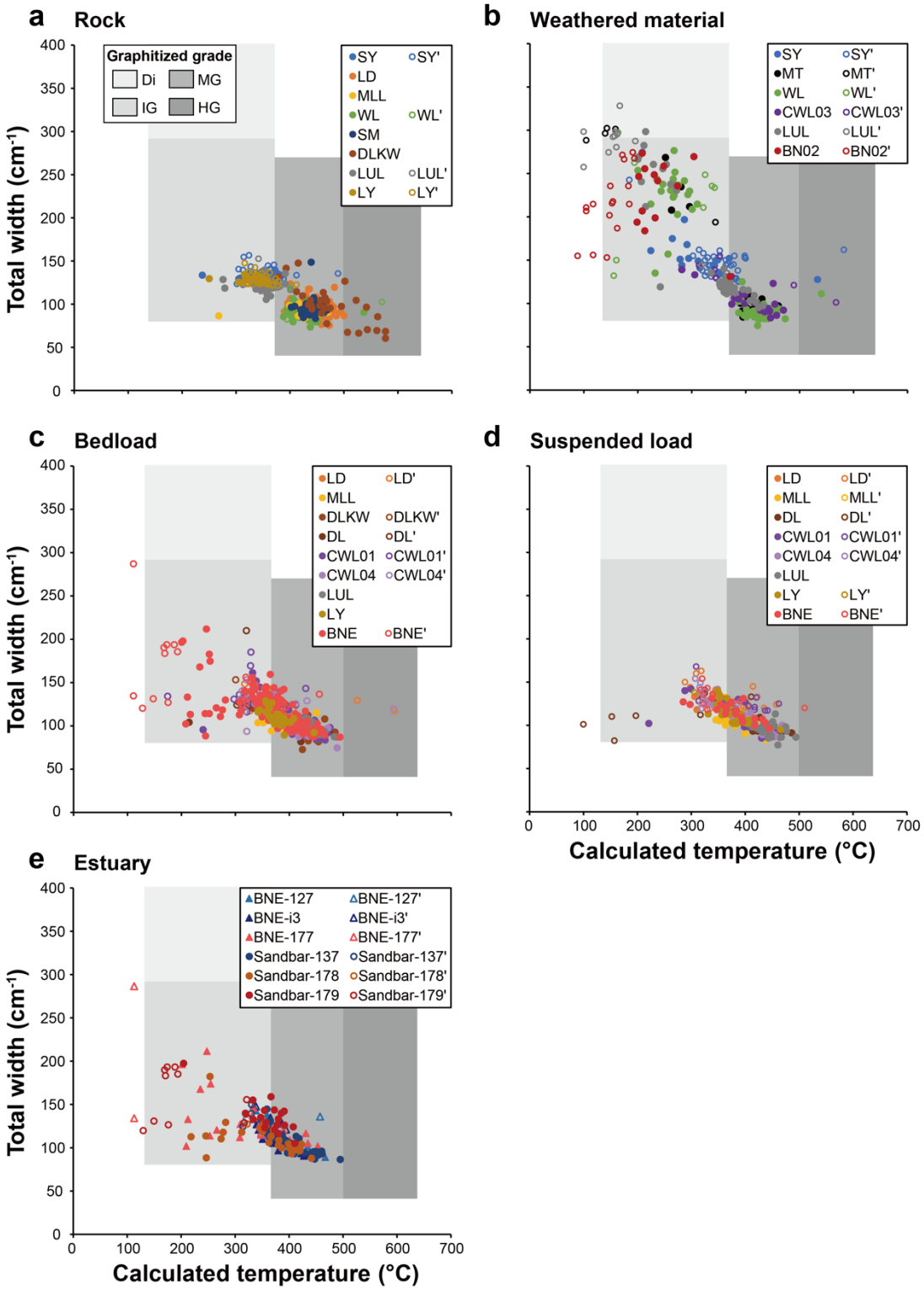

Fig. S2. Plots of total width vs. calculated temperature for OC_{petro}.

Data points with metamorphic temperature out of the calculation limit are in open circles, and those within the range are in solid circles. Sample types include rock **a**, weathered material **b**, bedload **c**, suspended load **d** and estuary **e**. Di, IG, MG and HG coded with colors in **a** stand for the Disordered, Intermediate-Grade, Mildly Graphitized and Highly Graphitized OC_{petro}, respectively, and are the same for the other sub-panels.

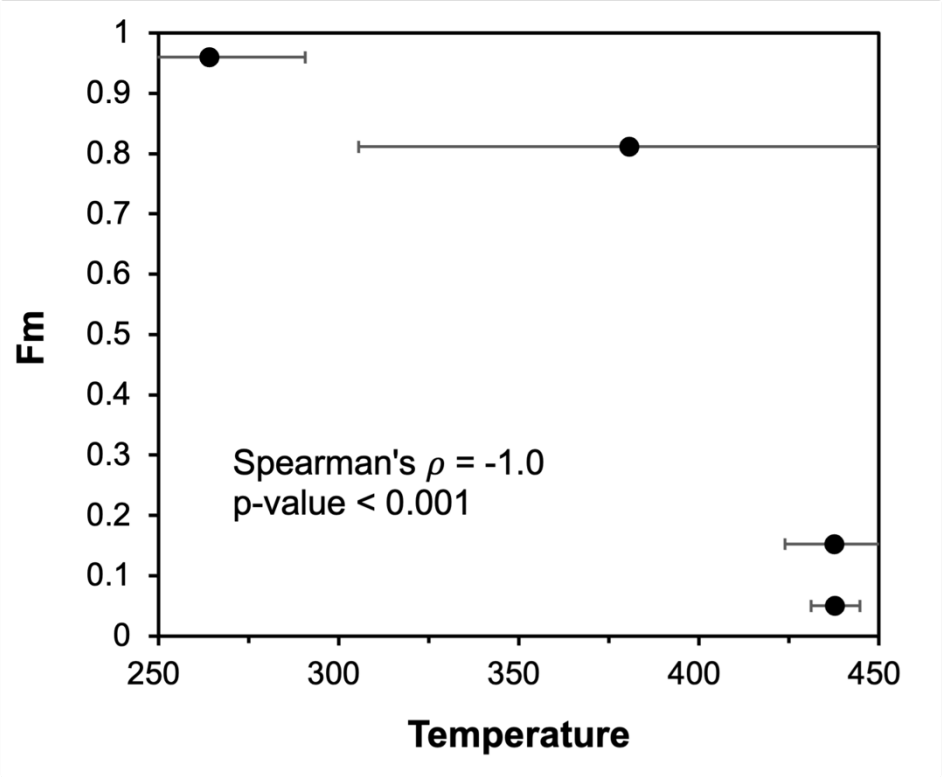

Fig. S3. The Fm value vs. temperature of OC_{petro} from the suite of weathered materials at WL.

The temperature is displayed as the average of all analyzed OC_{petro} (in calculation limit) in each sample. All error bars are shown as ± 1σ (details in Table S1). Fm: Fraction modern carbon.

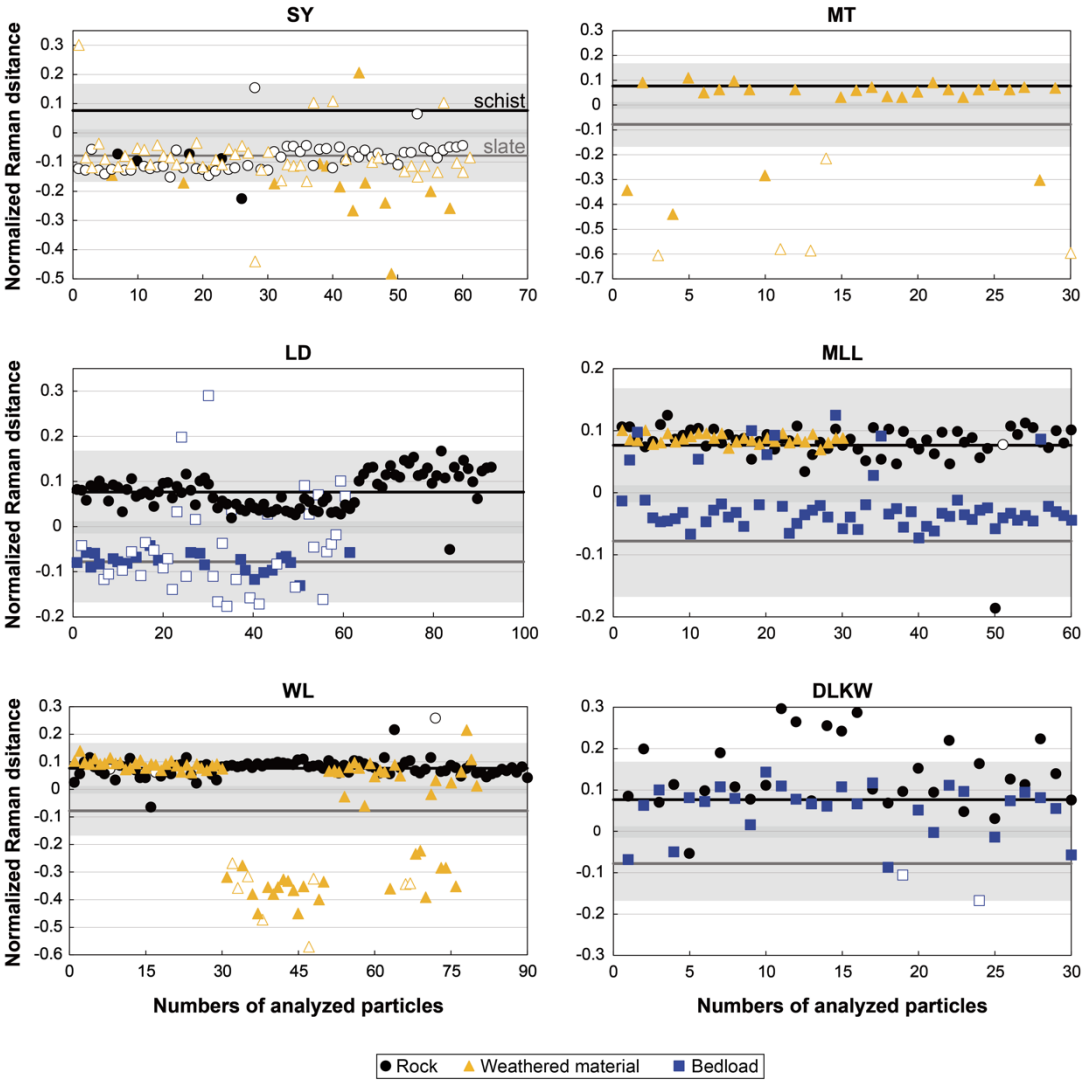

Fig. S4. Raman distance of samples at each location.

The mean normalized Raman distances of schists and slates are 0.08±0.09 (black line) and -0.08±0.09 (gray line), respectively, within one standard deviation in shaded areas. Black circles for rocks, yellow triangles for weathered materials, and blue squares for bedloads. Solid symbols are the samples with calculated temperatures in the estimation limit, and open symbols are those out of the range.

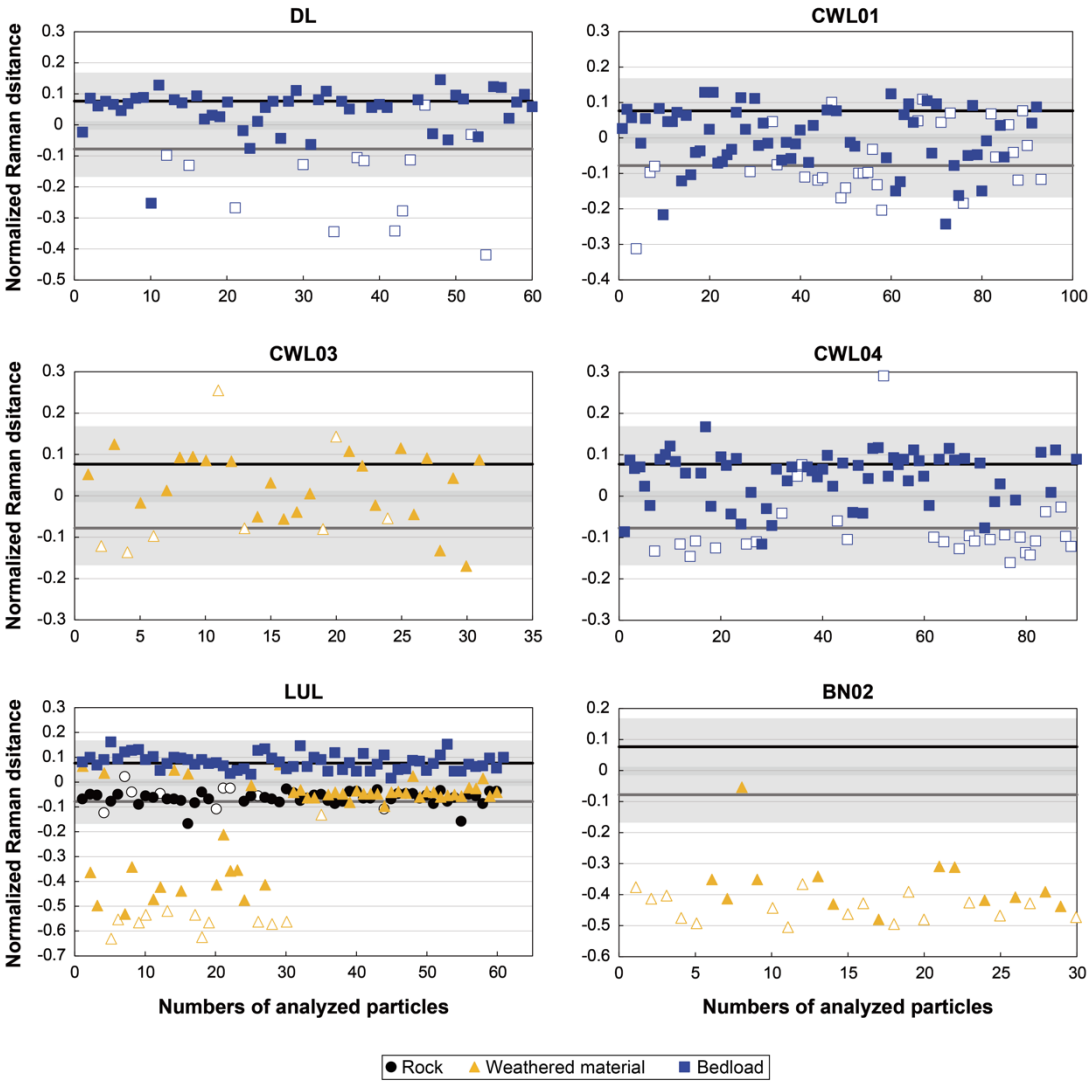

(Continued) Fig. S4.

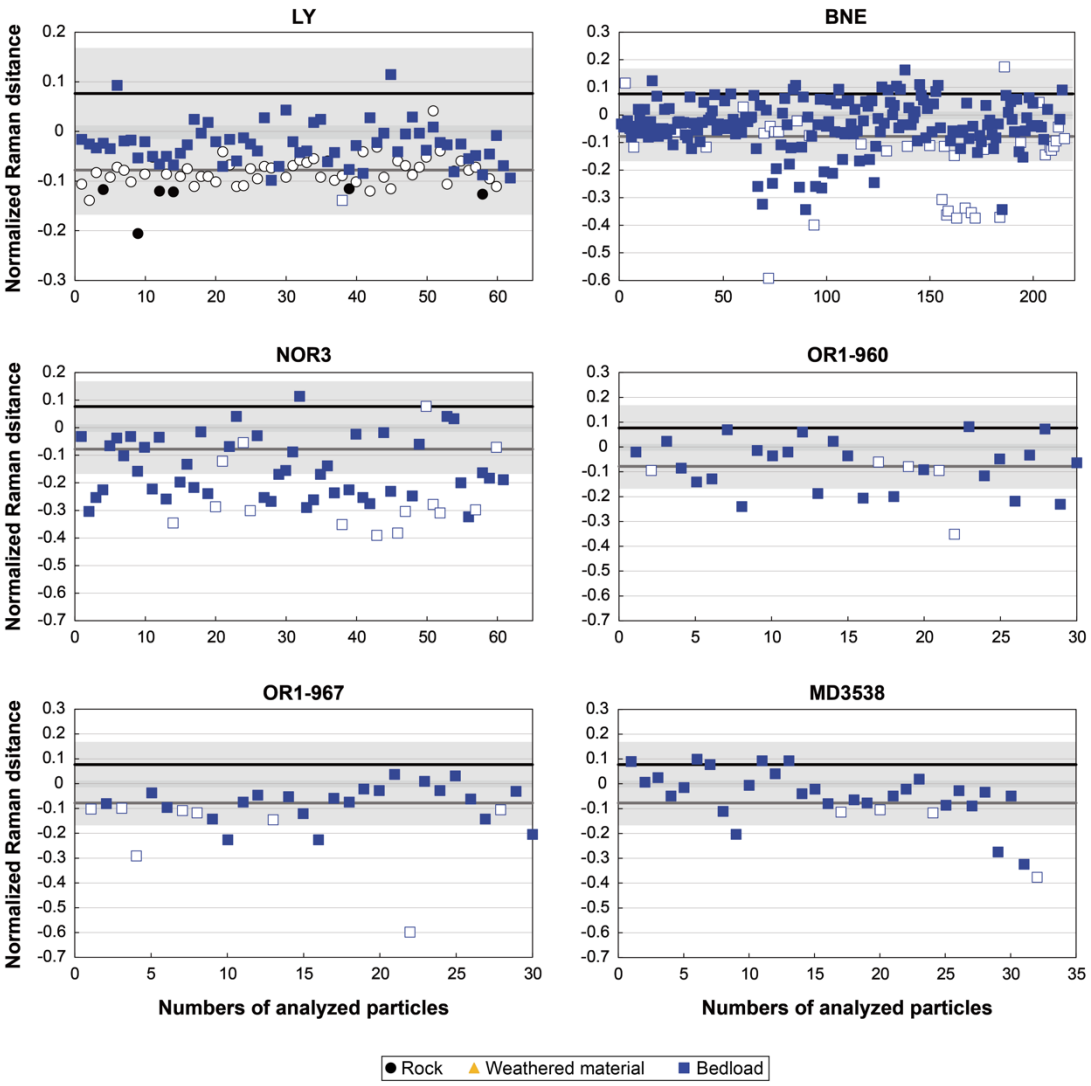

(Continued) Fig. S4.

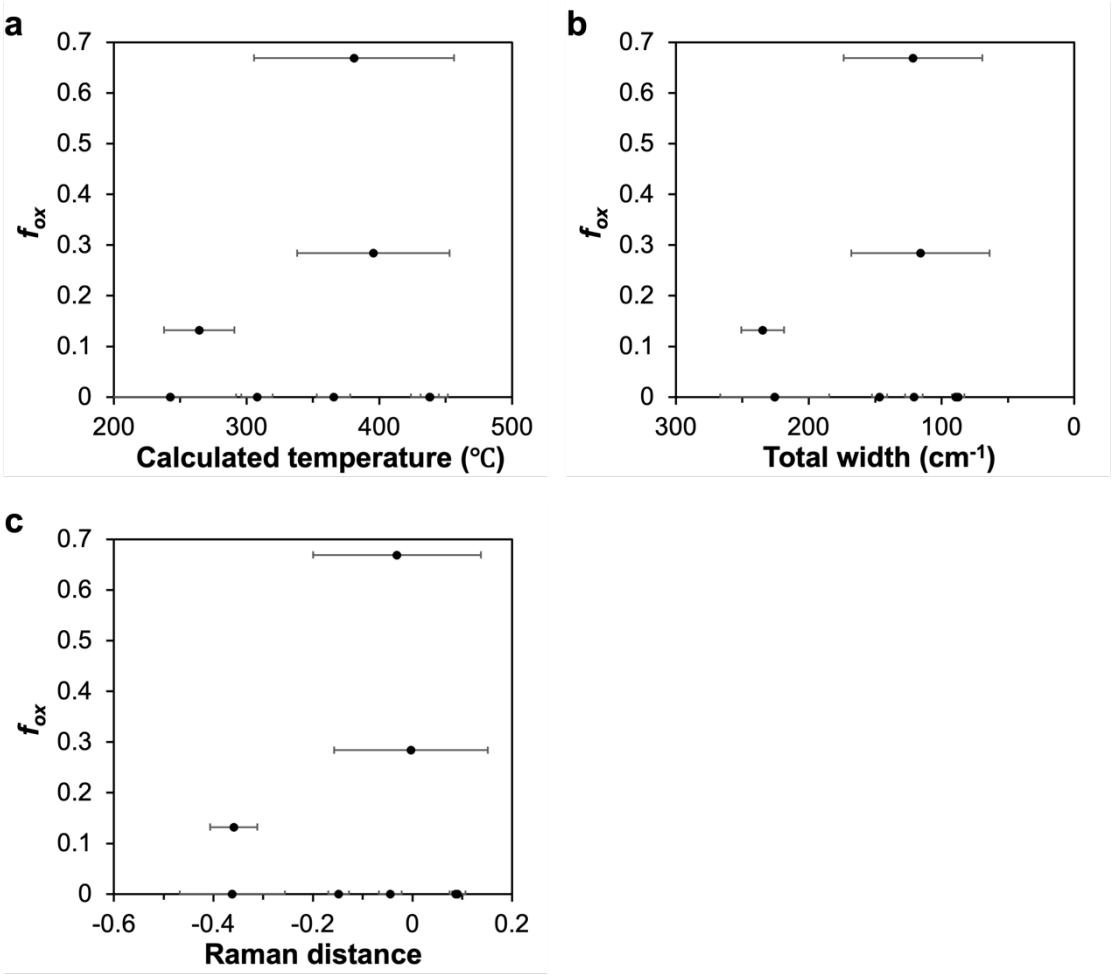

Fig. S5. Plots of f_{ox} vs. Raman parameter.

The Raman parameters include the derived temperature based on the relative area of D and G bands **a**, the total width of D and G bands **b**, and the Raman distance **c** based on the maturity difference assessed by the total width and derived temperature between individual analyzed particle versus the averaged rock characteristics. The f_{ox} values beyond reality (Fig. 6) are shown as zero. Error bars represent ± 1σ. f_{ox}: the oxidation fraction of OC_{petro}.

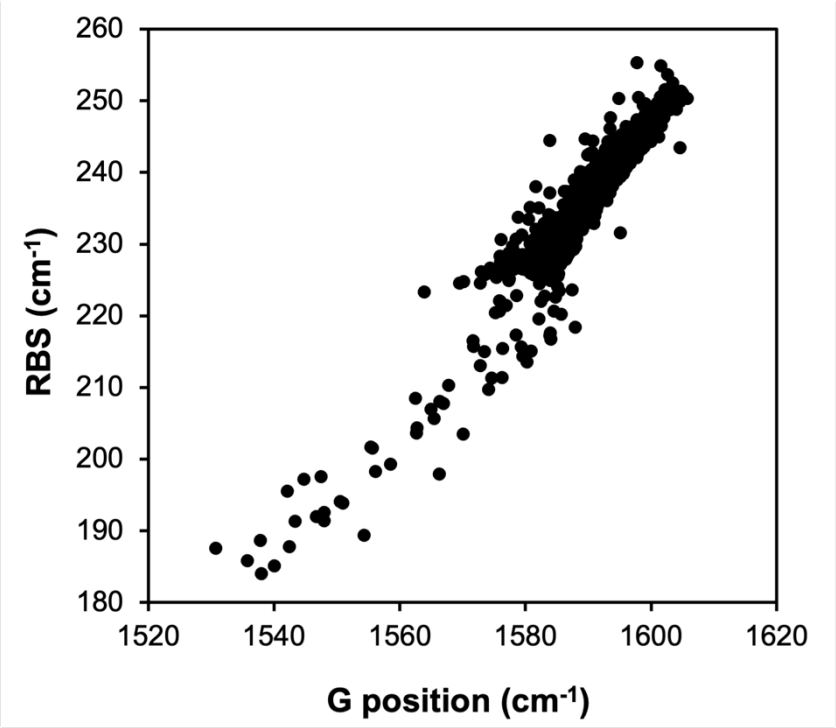

Fig. S6. Plot of Raman band separation (RBS) vs. G band position.
The RBS is defined as the position distance between the G and D1 bands.

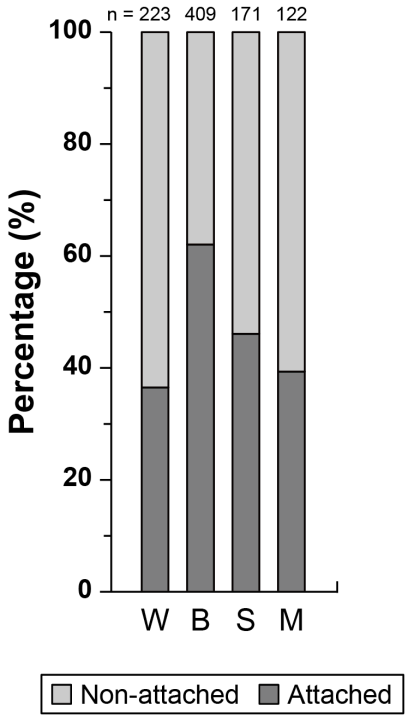

Fig. S7. Mineral-OC_{petro} associations in each compartment.

The mineral-OC_{petro} relationship is shown in two groups: non-attached (light gray) and attached (dark gray). The first group corresponds to either no mineral signals or unidentified signals during the acquisition of OC_{petro} spectra. The second group corresponds to the direct mineral-OC_{petro} association with minerals identifiable by current instrumentation setting. Possible occurrences of these two categories can be found in Method. W, B, S and M stand for weathered materials, bedload, suspended load and marine sediments, respectively. The percentage of non-attached group for rocks is ~30%, probably as a result of gentle grinding during sample preparation (n = 321).

Table S1. Details of sample information and analytical results for elemental and isotopic compositions.

Sample No.	Site	Sample type	Sample date	Longtitude	Latitude	TN (%)	TN SD	TOC (%)	TOC SD	C/N ratio	C/N SD	$\delta^{13}C$ (‰, VPDB)	Fm	Fm SD
164	SY	slate	2020/3/10	120°58'15.81"E	23°16'2.56"N	0.06	0.00	0.30	0.00	5.3	0.1	-25.0		
166	SY	slate	2020/3/10	120°57'40.83"E	23°15'51.05"N	0.10	0.00	0.61	0.01	6.0	0.2	-24.9		
167	SY	weathered material	2020/3/10	120°58'4.62"E	23°16'2.20"N	0.09	0.00	0.41	0.08	4.5	0.9	-23.4		
168	SY	weathered material	2020/3/10	120°58'30.03"E	23°16'20.13"N	0.12	0.00	0.91	0.01	7.4	0.1	-24.8	0.2584	0.0013
144	MT	weathered material	2020/1/14	121°1'6.56"E	23°12'7.54"N	0.29	0.00	2.22	0.00	7.8	0.1	-28.5	0.9455	0.0035
172	LD	meta-sandstone	2020/5/5	121°1'7.14"E	23°10'59.75"N	0.02	0.00	0.07	0.00	3.8	0.2	-20.5		
42	LD	meta-sandstone	2017/3/7	121°1'7.03"E	23°11'4.63"N	0.08	0.00	0.52	0.00	6.7	0.1	-18.2		
i1	LD	meta-sandstone	2020/5/5	121°1'6.71"E	23°10'59.80"N	0.15	0.01	0.79	0.03	5.3	0.3	-21.1		
s1	LD	suspended load	2019/7/24	121°1'8.33"E	23°11'1.17"N	0.09	0.00	0.62	0.01	7.1	0.4	-25.6		
136	LD	bedload	2019/7/24	121°1'8.33"E	23°11'1.17"N	0.05	0.00	0.24	0.00	4.6	0.1	-24.4		
176	MLL	schist	2020/5/5	121°2'1.86"E	23°10'15.49"N	0.11	0.00	0.64	0.01	5.9	0.2	-20.2		
s2	MLL	suspended load	2019/7/24	121°2'4.44"E	23°10'20.37"N	0.11	0.03	1.59	0.02	13.9	4.1	-27.2		
135	MLL	bedload	2019/7/24	121°2'4.44"E	23°10'20.37"N	0.03	0.00	0.22	0.00	6.4	0.3	-23.7		
147	WL	schist	2020/1/14	121°2'35.94"E	23°9'42.91"N	0.12	0.00	0.80	0.00	6.8	0.0	-17.2		
151	WL	schist	2020/1/15	121°1'50.39"E	23°9'56.02"N	0.14	0.00	0.73	0.00	5.1	0.1	-21.4		
174	WL	schist	2020/5/5	121°2'35.01"E	23°9'34.12"N	0.11	0.00	0.28	0.00	2.6	0.1	-22.5		
175	WL	schist	2020/5/5	121°2'32.74"E	23°9'34.35"N	0.09	0.00	0.15	0.00	1.6	0.0	-21.4		
145	WL	weathered material	2020/1/14	121°2'34.08"E	23°9'34.55"N	0.41	0.00	4.33	0.21	10.6	0.5	-23.9	0.9598	0.0036
148	WL	weathered material	2020/1/14	121°2'35.94"E	23°9'42.91"N	0.15	0.00	0.67	0.01	4.5	0.1	-22.0	0.1526	0.0011
150	WL	weathered material	2020/1/15	121°1'49.81"E	23°9'56.60"N	0.11	0.00	0.78	0.01	7.2	0.1	-16.6	0.0500	0.0006
173	WL	weathered material	2020/5/5	121°2'32.74"E	23°9'34.35"N	0.15	0.00	0.60	0.06	4.0	0.4	-21.5	0.8113	0.0030
152	SM	schist	2020/1/15	121°4'10.71"E	23°9'6.44"N	0.16	0.00	1.27	0.00	8.1	0.3	-21.7		
155	DLKW	schist	2020/1/13	121°2'59.21"E	23°7'28.15"N	0.01	0.00	0.07	0.01	5.5	1.3	-23.3		
157	DLKW	bedload	2020/1/15	121°3'0.72"E	23°7'30.72"N	0.25	0.00	1.71	0.01	6.8	0.1	-23.3		
s3	DL	suspended load	2019/7/23	121°7'9.50"E	23°7'58.69"N	0.34	0.06	1.86	0.02	5.4	0.9	-25.3		
133	DL	bedload	2019/7/23	121°7'9.50"E	23°7'58.69"N	0.08	0.00	0.47	0.01	5.8	0.1	-22.5		
s4	CWL01	suspended load	2019/7/23	121°7'6.99"E	23°8'6.16"N	0.52	0.27	2.05	0.02	3.9	2.0	-25.0		
132	CWL01	bedload	2019/7/23	121°7'6.99"E	23°8'6.16"N	0.05	0.00	0.20	0.01	4.4	0.2	-24.0		
i2	CWL01	bedload	2020/5/5	121°7'6.99"E	23°8'6.16"N	0.03	0.00	0.11	0.02	4.4	0.6	-23.5		
142	CWL03	weathered material	2020/1/13	121°7'35.02"E	23°8'14.96"N	0.06	0.00	0.36	0.00	6.4	0.2	-24.0		
s5	CWL04	suspended load	2019/7/23	121°9'38.03"E	23°7'42.86"N	0.17	0.01	1.62	0.02	9.5	0.7	-25.2		
134	CWL04	bedload	2019/7/23	121°9'38.03"E	23°7'42.86"N	0.07	0.00	0.39	0.01	5.9	0.2	-22.9		
143	CWL04	bedload	2020/1/13	121°9'44.39"E	23°7'48.77"N	0.05	0.00	0.30	0.03	5.9	0.6	-22.7		
139	LUL	slate	2020/1/13	121°5'19.90"E	22°58'14.94"N	0.07	0.00	0.13	0.00	2.0	0.0	-26.0		
180	LUL	slate	2020/8/24	121°5'24.79"E	22°58'10.65"N	0.03	0.00	0.10	0.00	2.8	0.2	-24.3		
141	LUL	weathered material	2020/1/13	121°5'19.90"E	22°58'14.94"N	0.07	0.00	0.20	0.01	2.8	0.1	-23.8	0.1785	0.0009
171	LUL	weathered material	2020/5/4	121°5'26.83"E	22°58'11.59"N	0.69	0.01	7.65	0.39	11.1	0.6	-27.7		
s6	LUL	suspended load	2019/8/28	121°5'26.48"E	22°58'9.61"N	0.07	0.00	0.38	0.00	5.5	0.2	-20.9		
130	LUL	bedload	2019/7/23	121°5'26.48"E	22°58'9.61"N	0.04	0.00	0.23	0.00	5.9	0.0	-19.9		
170	BN02	weathered material	2020/5/4	121°8'52.41"E	22°54'17.72"N	0.09	0.00	0.52	0.01	5.7	0.2	-26.1	0.2398	0.0012
138	LY	slate	2020/1/13	121°3'26.72"E	22°52'39.87"N	0.13	0.00	0.84	0.00	6.3	0.0	-24.0		
169	LY	slate	2020/5/4	121°3'40.08"E	22°52'52.91"N	0.11	0.00	0.61	0.00	5.4	0.1	-24.0		
s7	LY	suspended load	2019/7/23	121°3'24.07"E	22°52'35.05"N	0.09	0.00	0.56	0.00	6.6	0.2	-24.2		
129	LY	bedload	2019/7/23	121°3'24.07"E	22°52'35.05"N	0.04	0.00	0.24	0.01	5.9	0.3	-21.2		
s8	BNE	suspended load	2019/7/23	121°10'14.28"E	22°45'49.54"N	0.34	0.14	0.99	0.01	2.9	1.2	-24.3		
127	BNE	bedload	2019/7/23	121°10'14.28"E	22°45'49.54"N	0.03	0.00	0.18	0.00	5.6	0.3	-21.2		
i3	BNE	bedload	2020/5/5	121°10'14.28"E	22°45'49.54"N	0.04	0.00	0.21	0.04	5.5	1.1	-22.5		
177	BNE	bedload	2020/8/24	121°10'14.28"E	22°45'49.54"N	0.04	0.00	0.27	0.01	6.5	0.1	-23.1		
137	BNE	bedload (sandbar)	2020/1/13	121°10'40.25"E	22°46'17.53"N	0.04	0.00	0.24	0.01	5.4	0.2	-22.0		
178	BNE	bedload (sandbar)	2020/8/24	121°10'39.82"E	22°46'17.22"N	0.04	0.00	0.23	0.00	6.3	0.3	-22.8		
179	BNE	bedload (sandbar)	2020/8/24	121°10'39.82"E	22°46'17.22"N	0.09	0.00	0.49	0.05	5.4	0.6	-24.0		
m1	NOR3-1	marine sediment	2020/7/6	121°11'5.4"E	22°42'11.7"N	0.08	0.00	0.37	0.03	4.4	0.3	-22.9		
m2	NOR3-1	marine sediment (trap)	2020/7/5–9/19	121°11'5.4"E	22°42'11.7"N	0.15	0.00	1.01	0.00	6.8	0.0	-22.7		
m3	OR1-0960-C5	marine sediment	2011/5/26	121°21'50.4"E	22°45'50.4"N	0.07	0.00	0.45	0.02	6.4	0.3	-23.2		
m4	OR1-0967-S1	marine sediment	2011/7/15	121°22'22.8"E	22°40'4.8"N	0.07	0.00	0.50	0.02	7.4	0.3	-24.1		
m5	MD18-3538-BC	marine sediment	2018/6/18	122°19'30.0"E	22°32'24.0"N	0.07	0.00	0.36	0.02	5.2	0.3	-22.4		

Supplementary References

1 Dellinger, M. *et al.* High rates of rock organic carbon oxidation sustained as Andean sediment transits the Amazon foreland-floodplain. *Proceedings of the National Academy of Sciences* **120**, e2306343120 (2023). https://doi.org:https://doi.org/10.1073/pnas.2306343120

2 Hovius, N., Stark, C. P., Chu, H. T. & Lin, J. C. Supply and removal of sediment in a landslide-dominated mountain belt: Central Range, Taiwan. *The Journal of Geology* **108**, 73-89 (2000). https://doi.org:https://doi.org/10.1086/314387

3 Yanites, B. J., Tucker, G. E., Mueller, K. J. & Chen, Y. G. How rivers react to large earthquakes: Evidence from central Taiwan. *Geology* **38**, 639-642 (2010). https://doi.org:https://doi.org/10.1130/G30883.1

4 Bagnold, R. A. An approach to the sediment transport problem from general physics. Report No. 422I, (1966).

5 Yanites, B. J. *et al.* Incision and channel morphology across active structures along the Peikang River, central Taiwan: Implications for the importance of channel width. *GSA Bulletin* **122**, 1192-1208 (2010). https://doi.org:https://doi.org/10.1130/b30035.1

6 Chim, L. K., Yen, J.-Y., Huang, S.-Y., Liou, Y.-S. & Tsai, L. L.-Y. Using Raman Spectroscopy of Carbonaceous Materials to track exhumation of an active orogenic belt: An example from Eastern Taiwan. *Journal of Asian Earth Sciences* **164**, 248-259 (2018). https://doi.org:https://doi.org/10.1016/j.jseaes.2018.06.030

7 Nibourel, L., Herman, F., Cox, S. C., Beyssac, O. & Lavé, J. Provenance analysis using Raman spectroscopy of carbonaceous material: A case study in the Southern Alps of New Zealand. *Journal of Geophysical Research: Earth Surface* **120**, 2056-2079 (2015). https://doi.org:https://doi.org/10.1002/2015JF003541

8 Deng, K. *et al.* Detrital zircon geochronology of river sands from Taiwan: Implications for sedimentary provenance of Taiwan and its source link with the east China mainland. *Earth-Science Reviews* **164**, 31-47 (2017). https://doi.org:https://doi.org/10.1016/j.earscirev.2016.10.015

9 Dadson, S. J. *et al.* Links between erosion, runoff variability and seismicity in the Taiwan orogen. *Nature* **426**, 648-651 (2003). https://doi.org:https://doi.org/10.1038/nature02150

10 Kao, S. J. & Milliman, J. D. Water and sediment discharge from small mountainous rivers, Taiwan: The roles of lithology, episodic events, and human activities. *The Journal of Geology* **116**, 431-448 (2008). https://doi.org:https://doi.org/10.1086/590921

11 Chen, C. Y., Willett, S. D., Christl, M. & Shyu, J. B. H. Drainage basin dynamics during the transition from early to mature orogeny in Southern Taiwan. *Earth and Planetary Science Letters* **562**, 116874 (2021). https://doi.org:https://doi.org/10.1016/j.epsl.2021.116874

12 Chen, T.-W. *et al.* Retro-Foredeep Basin Evolution in Taiwan: Zircon U-Pb and Hf Isotope Constraints From the Coastal Range. *Geochemistry, Geophysics, Geosystems* **24**, e2022GC010787 (2023). https://doi.org:https://doi.org/10.1029/2022GC010787

13 Morales, C. *et al.* In-situ study of the carbon gasification reaction of highly oriented pyrolytic graphite promoted by cobalt oxides and the novel nanostructures appeared after reaction. *Carbon* **158**, 588-597 (2020). https://doi.org:https://doi.org/10.1016/j.carbon.2019.11.030

14 Nair, S. S., Saha, T., Dey, P. & Bhadra, S. Thermal oxidation of graphite as the first step for graphene preparation: effect of heating temperature and time. *Journal of Materials Science* **56**, 3675-3691 (2021). https://doi.org:https://doi.org/10.1007/s10853-020-05481-x

15 Knauer, M., Carrara, M., Rothe, D., Niessner, R. & Ivleva, N. P. Changes in Structure and Reactivity of Soot during Oxidation and Gasification by Oxygen, Studied by Micro-Raman Spectroscopy and Temperature Programmed Oxidation. *Aerosol Science and Technology* **43**, 1-8 (2009). https://doi.org:10.1080/02786820802422250

16 Hemingway, J. D. *et al.* Microbial oxidation of lithospheric organic carbon in rapidly eroding tropical mountain soils. *Science* **360**, 209-212 (2018). https://doi.org:https://doi.org/10.1126/science.aao6463

17 Hilton, R. G., Gaillardet, J., Calmels, D. & Birck, J.-L. Geological respiration of a mountain belt revealed by the trace element rhenium. *Earth and Planetary Science Letters* **403**, 27-36 (2014). https://doi.org:https://doi.org/10.1016/j.epsl.2014.06.021